Draft version April 19, 2017
Typeset using LaTeX default style in AASTeX61

arXiv:1704.05101v1 [astro-ph.GA] 17 Apr 2017

DEEP SUBMILLIMETER AND RADIO OBSERVATIONS IN THE SSA22 FIELD. I. POWERING SOURCES AND Lyα ESCAPE FRACTION OF Lyα BLOBS

Y. Ao,[1,2] Y. Matsuda,[1] C. Henkel,[3,4] D. Iono,[1] D. M. Alexander,[5] S. C. Chapman,[6] J. Geach,[7] B. Hatsukade,[8] M. Hayes,[9] N. K. Hine,[10] Y. Kato,[1,11] R. Kawabe,[1] K. Kohno,[8] M. Kubo,[1] M. Lehnert,[12] M. Malkan,[13] K. M. Menten,[3] T. Nagao,[14] R. P. Norris,[15,16] M. Ouchi,[17] T. Saito,[18] Y. Tamura,[8,19] Y. Taniguchi,[20] H. Umehata,[20] and A. Weiss[3]

[1] *National Astronomical Observatory of Japan, 2-21-1 Osawa, Mitaka, Tokyo 181-8588, Japan*
[2] *Purple Mountain Observatory, Chinese Academy of Sciences, Nanjing 210008, China*
[3] *MPIfR, Auf dem Hügel 69, 53121 Bonn, Germany*
[4] *Astron. Dept., King Abdulaziz Univ., P.O. Box 80203, Jeddah 21589, Saudi Arabia*
[5] *Centre for Extragalactic Astronomy, Department of Physics, Durham University, South Road, Durham DH1 3LE, UK*
[6] *Dept. of Physics and Atmospheric Science, Dalhousie University, Halifax, NS B3H 4R2, Canada*
[7] *Centre for Astrophysics Research, University of Hertfordshire, Hatfield, AL10 9AB, UK*
[8] *Institute of Astronomy, The University of Tokyo, 2-21-1 Osawa, Mitaka, Tokyo 181-0015, Japan*
[9] *Stockholm University, Department of Astronomy and Oskar Klein Centre for Cosmoparticle Physics, AlbaNova University Centre, SE-10691, Stockholm, Sweden*
[10] *Centre for Astrophysics Research, School of Physics, Astronomy and Mathematics, University of Hertfordshire, College Lane, Hatfield, Hertfordshire AL10 9AB, UK*
[11] *Department of Astronomy, Graduate school of Science, The University of Tokyo, 7-3-1 Hongo, Bunkyo-ku, Tokyo 133-0033, Japan*
[12] *Institut d'Astrophysique de Paris, CNRS and Université Pierre et Marie Curie, 98bis Bd Arago, 75014 Paris, France*
[13] *Department of Physics & Astronomy, University of California, Los Angeles, CA 90095, USA*
[14] *Research Center for Space and Cosmic Evolution, Ehime University, Bunkyo-cho 2-5, Matsuyama, Ehime 790-8577, Japan*
[15] *CSIRO Australia Telescope National Facility, PO Box 76, Epping, NSW 1710, Australia*
[16] *Western Sydney University, Locked Bag 1797, Penrith South, NSW 1797, Australia*
[17] *Institute for Cosmic Ray Research, The University of Tokyo, 5-1-5 Kashiwa-no-Ha, Kashiwa City, Chiba 277-8582, Japan*
[18] *Nishi-Harima Astronomical Observatory, Centre for Astronomy, University of Hyogo, 407-2 Nichigaichi, Sayo-cho, Sayo, Hyogo 679-5313, Japan*
[19] *Department of Physics, School of Science, Nagoya University, Furo-cho, Chikusa-ku, Nagoya, Aichi 464-8602, Japan*
[20] *The Open University of Japan, 2-11, Wakaba, Mihama-ku, Chiba, 261-8586, Japan*

ABSTRACT

We study the heating mechansims and Lyα escape fractions of 35 Lyα blobs (LABs) at $z \approx 3.1$ in the SSA22 field, using the submillimeter (submm) data from the Atacama Large Millimeter/Submillimeter Array (ALMA) and the Submillimetre Common-User Bolometer Array-2 (SCUBA-2) on the James Clerk Maxwell Telescope (JCMT), and the radio data from the Karl G. Jansky Very Large Array (VLA). With ALMA and JCMT/SCUBA-2, we have identified dust continuum sources in 11 out of 35 LABs in the SSA22 field, with star formation rates (SFRs) of above $100 M_\odot$/yr. Using VLA, we have detected likely radio counterparts in 9 out of 29 LABs in the SSA22 field. The detection of submm dust emission in LABs is more linked to the physical sizes of the Lyα emission than to the Lyα luminosities of LABs. The results may indicate that more massive galaxies tend to be formed in the LABs with large Lyα spatial extents, and also suggest that most massive galaxies tend to reside in the centers of protoclusters. We find that a radio excess in the submm/radio detected LABs is common, suggesting that active galactic nuclei (AGN) may often be present in these systems. Most radio sources without X-ray counterparts are located in the centers of the LABs. However, it is surprising that all X-ray counterparts avoid the central regions of their LABs. Possibly these X-ray sources are associated with merging systems, which re-distribute the interstellar meidium (ISM) and circumgalactic medium (CGM), leading to highly inhomogeneous gas. Alternatively, AGN and its feedback may also be responsible for inhomogeneous Lyα morphology in these LABs. We obtain escape fractions of Lyα photons

for the LABs based on the submm and Lyα data, and find that the Lyα escape fractions in the LABs are significantly lower than those found for Lyα emitters (LAEs) in other studies. We suspect that this large difference is due to the SCUBA-2 detection threshold, the high dust attenuation indicated by the large SFRs in our sample, as well as the dense large-scale environment in SSA22.

Keywords: galaxies: formation – galaxies:high-redshift – galaxies:ISM – galaxies:active – infrared:galaxies

1. INTRODUCTION

Lyα emission has emerged as a powerful tool to study distant galaxies, as it is very bright and redshifted to optical wavelengths at high redshifts. Lyα emitters (LAEs), efficiently discovered in narrowband imaging surveys, are galaxies that emit strong Lyα radiation presumably from the photoionization of neutral hydrogen by young, hot stars or AGN at high redshifts. They hold unique clues to the formation and evolution of galaxies at a time when the Universe was still young (e.g. Bridge et al. 2013). However, due to the resonant nature of the Lyα line and high optical depth in neutral hydrogen (Hayes 2015), Lyα photons are likely to undergo numerous scattering events before they escape from the galaxy or are absorbed by dust. Thus the actual emitted Lyα luminosity is a function of the atomic hydrogen distribution, dust content, gas kinematics and galaxy viewing angle (Hayes 2015). Therefore, in order to use Lyα to study galaxies at high redshift, we need to understand the escape fraction of Lyα photons, which is defined as the ratio of observed to intrinsic Lyα luminosity and thus determined by the Lyα emitter's environment. The evolution of the Lyα escape fraction over cosmic time has been determined based on empirical measurements from large samples (e.g., Gronwall et al. 2007; Ouchi et al. 2008; Hayes et al. 2011a), providing useful clues to the evolution of the dust content of galaxies.

As a special class of LAEs, Lyα blobs (LABs) have been most commonly found in the dense environment of star-forming galaxies at high redshift and are characterized by their large physical scale (30 to 200 kpc) and high Lyα luminosity (10^{43} to 10^{44} erg s^{-1}) (see e.g., Francis et al. 1996; Steidel et al. 2000; Palunas et al. 2004; Matsuda et al. 2004, 2009, 2011, 2012; Dey et al. 2005; Saito et al. 2006; Yang et al. 2009, 2010; Erb et al. 2011; Prescott et al. 2012a, 2013; Bridge et al. 2013; Xue et al. 2017). While the LABs' preferential location in overdense environments indicates an association with massive galaxy formation, the origin of their Lyα emission is still unclear and under debate (Faucher-Giguere et al. 2010; Cen & Zheng 2013; Yajima et al. 2013). Proposed sources have generally fallen into two categories: (1) cooling radiation from cold streams of gas accreting onto galaxies (e.g., Haiman et al. 2000; Dijkstra & Loeb 2009; Faucher-Giguère et al. 2010) and (2) photoionization and/or galactic super-winds/outflows from starbursts or AGN (e.g., Taniguchi & Shioya 2000; Furlanetto et al. 2005; Wilman et al. 2005; Colbert et al. 2006; Mori & Umemura 2006; Matsuda et al. 2007; Zheng et al. 2011; Cen & Zheng 2013; Ao et al. 2015; Prescott et al. 2015; Alexander et al. 2016; Hine et al. 2016). All of the above mentioned energy supplying sources may trigger Lyα emission in an environment where violent interactions are frequent between gas rich galaxies as expected in over-dense regions at high redshift (Matsuda et al. 2009, 2011; Prescott et al. 2012b; Kubo et al. 2013).

Supporting evidence for the cooling flow scenario comes from those LABs lacking any visible power source (e.g., Smith & Jarvis 2007). Dijkstra & Loeb (2009) propose that the sources associated with the LABs may have little to do in powering the spatially extended Lyα emission because recent hydrodynamical simulations of galaxy formation show that baryons assemble into galaxies through a two-phase medium, which contains filamentary streams of cold ($T \sim 10^4$ K) gas embedded within a hotter gaseous halo (e.g. Kereš et al. 2005; Dekel et al. 2009). The cold streams are probable sources of spatially extended Lyα emission. This model can naturally explain the spatial distribution of the LABs and the diversity of host galaxies in the LABs, as the Lyα emission is effectively decoupled from the associated sources. The most luminous gravitationally powered blobs would be associated with the most massive halos, which can host a variety of sources like active galactic nuclei (AGN), Lyman Break Galaxies (LBGs) and Submillimeter Galaxies (SMGs). Alternatively, ionizing photons from young stars in star-forming (SF) galaxies and/or unobscured AGN can ionize neutral hydrogen atoms and the subsequent recombination leads to Lyα emission. It is usually difficult to discriminate between the two internal heating mechanisms, SF or AGN. Resonant scattering of Lyα photons in the circumgalactic medium leads to spatially extended emission (Geach et al. 2005, 2009; Colbert et al. 2006; Webb et al. 2009; Hayes et al. 2011b; Zheng et al. 2011; Cen & Zheng 2013; Overzier et al. 2013). Cen & Zheng (2013) propose an SF-based model and predict that LABs at high redshift correspond to protoclusters containing the most massive galaxies/halos in the universe and ubiquitous strong infrared (IR) sources undergoing extreme starbursts. Their model also predicts that the most luminous FIR source within each LAB is likely representing the gravitational center of the protocluster. Note that both cooling flow (Dijkstra & Loeb 2009) and SF-based models (Cen & Zheng 2013) can reproduce the measured luminosity functions of LABs.

To study the heating mechanism(s) of the LABs and investigate their Lyα escape fraction, we need to select a large sample of LABs to locate their accurate positions and investigate their possible powering sources. SSA22 is such a suitable field because it has 35 LABs detected at $z \approx 3.1$ (Matsuda et al. 2004), providing an ideal laboratory to study the LABs in a large sample. One of them, SSA22-LAB01 is the best studied source (e.g., Matsuda et al. 2007; Yang et al. 2012; Geach et al. 2014, 2016; Umehata et al. 2017a). At (sub)mm wavelength, most LABs of SSA22

have been studied with the Submillimetre Common-User Bolometer Array (SCUBA, Geach et al. 2005) and SCUBA-2 (Hine et al. 2016) on the James Clerk Maxwell Telescope (JCMT), and with the AzTEC 1.1 mm camera (Tamura et al. 2009, 2013; Umehata et al. 2014) on the Atacama Submillimeter Telescope Experiment (ASTE). However, no significant 1.1 mm continuum has been found in any of individual 35 LABs (Tamura et al. 2013). Even in the recent deep SCUBA-2 observations, only two out of 34 LABs are detected at 850 μm (Hine et al. 2016). A few LABs have been observed and detected in the dust continuum with the Atacama Large Millimeter/Submillimeter Array (ALMA; Umehata et al. 2015; Alexander et al. 2016; Geach et al. 2016). In this paper, we present deep submm results from new JCMT/SCUBA-2 data (Holland et al. 2013) together with ALMA data, and deep radio images from the Karl G. Jansky Very Large Array (VLA)[1] observations to study the LABs in the SSA22 field. Note that in this paper we only focus on the LABs; the SMGs in this region will be presented in an upcoming paper based on the same submm and radio data (Ao et al. in preparation).

2. OBSERVATIONS

2.1. *JCMT/SCUBA-2 observations*

The observations were carried out at 850 μm with SCUBA-2 (Holland et al. 2013) at the JCMT. The data were taken between April 20 and June 30 in 2015 under good weather conditions when the zenith optical depth at 225 GHz was in the range $0.04 < \tau_{225} < 0.08$ with a mean $< \tau_{225} >$ of 0.06. We observed a subregion of SSA22 with a total on-source observing time of 19 hours, covering a field with a diameter of 15 arcmin, centered on $\alpha(\mathrm{J2000}) = 22^{\mathrm{h}}17^{\mathrm{m}}31^{\mathrm{s}}.7$, $\delta(\mathrm{J2000}) = +00^{\mathrm{o}}17'50''$, using multiple repeats (40 mins per repeat) of the PONG scanning patter (Holland et al. 2013). The SSA22 field was also observed as part of the JCMT SCUBA-2 Cosmology Legacy Survey (S2CLS, Hine et al. 2016; Geach et al. 2017) with a total on-source observing time of 72 hours to cover a map with a diameter of 30 arcmin, centered on $\alpha(\mathrm{J2000}) = 22^{\mathrm{h}}17^{\mathrm{m}}36^{\mathrm{s}}.3$, $\delta(\mathrm{J2000}) = +00^{\mathrm{o}}19'22''.7$. The observations are summarized in Table 1.

Pointing checks and flux calibration were achieved via observations of Neptune and Uranus, immediately before and after the science exposures. Data reduction was carried out using the SubMillimeter User Reduction Facility (smurf) *makemap* pipeline (Chapin et al. 2013), with flat-fields, image stacking, and removing atmospheric emission (see also Hine et al. 2016 for more details). The main beam size of SCUBA-2 observations at 850 μm is $13''$ and the map is convolved with a smoothed beam of $30''$ to optimize the detection of point sources. The total on-source integration time was about 91 hours (see Table 1). The final beam-convolved map reaches an rms noise level of 0.75 mJy/beam within the central 15 arcmin and about 1.0 mJy/beam outside the central region (see Figure 1).

2.2. *ALMA observations*

ALMA observations were carried out in band 7 with a central frequency of 350 GHz towards 4 LABs (LAB1, LAB2, LAB5 and LAB18) (project code: 2013.1.00704S; Matsuda et al. in preparation). Another two LABs, LAB12 and LAB14, had been covered by a deep field in SSA22 (Umehata et al. 2015, 2017b) in band 6 with a central frequency of 263 GHz. The data were reduced with the CASA package in a standard manner (for the details see Umehata et al. 2017b and Matsuda et al. in preparation).

2.3. *VLA observations*

We observed the SSA22 region centered around the location of our SCUBA-2 observations with the VLA in B-configuration at S-band (2-4 GHz), under projects 15A-120 and 16A-310. During 17 sessions with a total observing time of 41 hours, we observed three positions in 2015 and 2016 (see Table 1 for the observing log). The total bandwidth was 2 GHz, split in 16 spectral windows.

Data were first processed through the VLA Common Astronomy Software Applications (CASA) Calibration Pipeline by NRAO staff, performing basic flagging and calibration. Then we iteratively inspected the data, and then flagged the data with radio frequency interference. The final mosaic of images was created with CASA task CLEAN, reaching an rms sensitivity of 1.5 μJy/beam (before primary beam correction) and an angular resolution of $2.3''\times2.0''$. The primary beam of one single pointing is about 15 arcmins. In Figure 2, we shows 29 out of the 35 LABs identified by Matsuda et al. (2004) in the final radio image.

3. RESULTS

[1] The National Radio Astronomy Observatory is a facility of the National Science Foundation operated under cooperative agreement by Associated Universities, Inc.

3.1. *Submm emission*

For the 35 LABs identified in Matsuda et al. (2004), all sources are covered by SCUBA-2 observations, as shown in Figure 1. The SSA22 field has been observed as part of the JCMT S2CLS project (Geach et al. 2017), reaching a 1σ level of 1.1 mJy/beam at 850 μm. Combined with our SCUBA2 observations in 2015, we reach a deeper rms sensitivity of about 0.75 mJy/beam for the overlapping region.

The SCUBA-2 850 μm flux measurements are listed in Table 2. 9 out of 35 LABs are detected in dust emission with peak SNRs above 2.5σ, and 6 of them above 3σ (see Figure 3). The three sources, LAB4, LAB9 and LAB14, with only marginal detection levels of 2.5σ have all been detected in the radio above 5σ.

Figure 4 shows the SCUBA-2, VLA and ALMA images together to cross check the detections with low significance from the SCUBA-2 and VLA observations by the highly significant ones from ALMA. The typical pointing accuracy of the JCMT is about 1-2″. Due to the noise of the image, the positional uncertainty of the SCUBA-2 observations is related to its signal-to-noise ratio (SNR) and beam size (Condon et al. 1998) via $\sigma_{\rm p} = \frac{\theta_{\rm beam}}{\rm SNR\ (2ln2)^{0.5}}$, where $\sigma_{\rm p}$ is the 1-σ positional uncertainty and $\theta_{\rm beam}$ the beam size. For a marginally detected source with an SNR of 3 and a smoothed beam of 30″, its positional uncertainty will be about 8.5″. Six LABs observed by ALMA have been detected with high SNRs. Two sources, LAB2 and LAB12, have not been detected with SCUBA-2 due to low flux densities, but have been detected with ALMA in the dust continuum. For the remaining four LABs, their positions are consistent with our SCUBA-2 observations if considering the positional uncertainties of SCUBA-2 observations. The VLA positions of the radio emission are in good agreement with those of the dust emission obtained with ALMA. These consistent results support the reliability of the SCUBA-2 and VLA data, even for the marginal detections. Adopting the number count study of SCUBA-2 sources in Geach et al. (2017), the probability of finding a 850 μm source with a flux greater than 2 mJy within a box of 15″, accounting for the typical LAB's size and the SCUBA-2's beam size at 850μm, is $\sim$5.2%. Thus, we expect to have two spurious submm sources detected above 2mJy among the 35 LABs in the SSA22 field. However, all SCUBA-2-detected sources have significant radio counterparts except for LAB10 and LAB11. The former is not covered by the VLA observations and the latter has a weak radio counterpart. Thus, all SCUBA-2 sources are very likely associated with the LABs, instead of a projection effect by chance.

3.2. *Radio emission*

In Figure 2, we show the full radio map imaged by the VLA observations with the radio emission in grey scale. 29 sources are covered by our observations, and 7 (LAB13, LAB15, LAB21, LAB22, LAB27, LAB28 and LAB33) of them are outside of the central Field of View (FoV) with a noise level of above $\sim$3.5 μJy/beam after primary beam correction. None of the sources outside of the FoV are detected at radio wavelengths, and this could be due to the poor sensitivities in these regions. Among the remaining 22 LABs, 9 are detected above 4σ. The VLA S band flux measurements are listed in Table 2. For 5 out of 9 radio detected sources, spectroscopic data at the same locations as the radio counterparts from the literatures show that their redshifts are around 3.1 (see Table 2). Adopting the number count study of radio sources in Condon et al. (2012), the probability of finding a 3 GHz source with a flux greater than 7.5 μJy within a typical LAB's size of 6″ is $\sim$4.2%. Thus, among the 22 sources with good sensitivities, we expect to have one spurious radio source detected above 7.5 μJy within the LABs.

3.3. *Star formation rates*

Here we derive the star formation rates (SFRs) from the Lyα, IR and radio luminosities. To estimate the SFR from the Lyα luminosity, we first assume that star formation (SF) powers the observed Lyα flux. We use an unreddened Lyα/Hα ratio of 8.7:1 and the conversion factor between Hα luminosity and SFR (Kennicutt 1998; Kennicutt & Evans 2012), yielding $\rm SFR(Ly\alpha)/(M_\odot/yr) = 0.62\ \times\ L_{Ly\alpha}/(10^{42}\ erg\ s^{-1})$. This provides a lower limit, because the dust extinction of Lyα emission, likely exacerbated by resonance scattering, may significantly reduce the observed Lyα luminosity.

For another estimate of the SFR, we first need to determine the IR luminosity. However, the dust SEDs of the LABs cannot be well constrained, as only one or two measurements at (sub)millimeter wavelength are available. Therefore, we will follow the method described in Umehata et al. (2015) to use the SED templates of well studied starburst galaxies, Arp 220 and M82 (Silva et al. 1998), a composite SED of SMGs from the ALESS (Swinbank et al. 2014), and SMM J21350201 (the cosmic eyelash; Swinbank et al. 2010) to consider a variety of SEDs. We created best fit SEDs for each template based on redshift and SCUBA-2/ALMA measurements. The spectra between 8 and 1000 μm in the rest frame were integrated, and we derive a median value as well as minimum/maximum values. Following the star

formation rate calibration in Kennicutt (1998) and Kennicutt & Evans (2012), we can estimate the SFR by using the relation $\mathrm{SFR}(L_{\mathrm{FIR}})/(\mathrm{M}_\odot/\mathrm{yr}) = 1.46\times L_{\mathrm{FIR}}/(10^{10}\ L_\odot)$. The uncertainties of submm-derived SFRs mainly come from the choice of adopted templates, and the minimum and maximum as well as median values are given in Table 3.

In luminous galaxies, radio emission is dominated by synchrotron radiation from electrons, and one can relate the SFR by the relation $\mathrm{SFR}(L_{1.4\ \mathrm{GHz}})/(\mathrm{M}_\odot/\mathrm{yr}) = 5.52\times10^{-22}\ L_{1.4\ \mathrm{GHz}}/(\mathrm{W\ Hz^{-1}})$ (Bell 2003). The radio luminosity at 1.4 GHz at the rest frame can be estimated from the observed flux at 3 GHz by assuming a relation $S \propto \nu^{\alpha}$, where S is the flux density and a typical spectral index commonly adopted for SMGs (e.g., Ivison et al. 2010) is $\alpha = -0.8$. The star formation rates derived using these three methods are listed in Table 3.

3.4. *Comments on individual LABs*

Radio data are not only helpful to discover the powering sources, but also to give the accurate positions of the unresolved SCUBA-2-detected sources and help to cross-identify and even verify the corresponding dust emission at a relatively faint detection level. Here, we will briefly describe the sources detected at submm and radio wavelengths. Deep X-ray observations with *Chandra* are available for the SSA22 field (Geach et al. 2009; Lehmer et al. 2009), and will also be discussed for the detected sources. For those readers mainly interested in statistically relevant results, we recommend continuing with § 4.

3.4.1. *LAB1*

For LAB1, the ALMA observations at 850 μm reveal three cores with a total flux density of 1.72±0.21 mJy (upper left panel in Figure 4; see also Geach et al. 2016 and Matsuda et al. 2017), two close to VLA-LAB1a and one close to VLA-LAB1b. Using the SCUBA-2 data, Geach et al. (2014) found a flux density of 4.6±1.1 mJy. Not accounting for the slightly different SCUBA-2 and ALMA primary beams, this suggests that 63±10% of the extended emission is missed by the ALMA observations. Combining this with new SCUBA-2 data, we find a flux density of 2.9±0.8 mJy, indicating that missing flux accounts for 41±15% of the total flux density. Considering the flux uncertainties, the new value is only slightly higher than ALMA's measurement, showing that in this LAB there may be not much extended structure missed by ALMA.

Two radio sources are detected in this LAB. The northern radio source, VLA-LAB1a, peaks at a location close to two dust continuum peaks, ALMA-LAB1a and ALMA-LAB1b. The southern radio source, VLA-LAB1b, is consistent with one of the ALMA 350 GHz continuum sources, ALMA-LAB1c. Weak X-ray emission is detected around the southern source. [CII] emission has also been detected in ALMA-LAB1b with a secured redshift of 3.0993±0.0004 (Umehata et al. 2017b).

3.4.2. *LAB2*

Radio emission is detected within this LAB. However, SCUBA-2 observations show no dust emission around this source down to a sensitivity of 0.8 mJy/beam. Sensitive ALMA observations find a counterpart near the radio source with a flux density of 0.91±0.10 mJy at 350 GHz, coincident with the X-ray counterpart (Geach et al. 2009).

Our observation doesn't confirm another continuum source (see Figure 4) marginally detected by Alexander et al. (2016) with a flux of 1.11±0.25 mJy, which is significantly higher than our 3 σ upper limit of 0.23 mJy. This may be due to the presence of extended structure that is resolved out by our higher angular resolution observations or it may be a spurious source.

3.4.3. *LAB3*

The VLA data show a tentative detection within this LAB, but no dust emission is detected with SCUBA-2. Note that the radio peak has only a 3σ significance, and there are no counterparts at other wavelengths. Thus, the VLA signal might not be reliable, and we consider this LAB as undetected at radio frequencies. A strong X-ray source is detected in this LAB, however it is not coincident with the weak radio peak.

Recently, dust continuum has been marginally detected around this LAB with ALMA (Alexander et al. 2016), but it is outside of the LAB, offset ∼4.5 arcsec (∼30 kpc) from the center. Thus, the dust continuum is not considered to be associated with the LAB.

3.4.4. *LAB4*

The radio emission peaks at the center of the LAB. However, the SCUBA-2 submm source is offset 9 arcsec from the center. Considering the positional uncertainty of about 9 arcsec for this weak source, we still consider the submm

source is consistent with the radio source and also associated with the LAB. A similar situation is encountered in LAB14, where the ALMA observations confirm the association between the radio and submm sources.

3.4.5. *LAB5*

This LAB is detected by SCUBA-2 and the VLA, and further confirmed by the ALMA observations. The SCUBA-2 and ALMA data show similar flux densities for this LAB.

3.4.6. *LAB9*

This LAB shows dust emission around the center. The VLA data reveal two radio components within this source, but only one source with an SNR above 4σ.

3.4.7. *LAB10*

This source is detected at submm wavelengths with a significance of 3σ by SCUBA-2, but is not covered by our radio observations. Further cross-identification is needed to confirm its reliability.

3.4.8. *LAB11*

This LAB shows SCUBA-2 dust emission around the center. The marginally detected radio emission shows elongated structure, and its reality needs to be confirmed because of its low SNR.

3.4.9. *LAB12*

A significant radio detection is found within the LAB, but no dust counterpart is detected by SCUBA-2. However, the more sensitive ALMA observations at 1.14 mm show dust emission around the radio source. It also coincides with a strong X-ray counterpart (Geach et al. 2009).

3.4.10. *LAB14*

The radio emission peaks around the center of the LAB, and SCUBA-2 show dust emission centered 7 arcsec off the radio peak. However, the ALMA observations demonstrate that the dust emission coincides with the radio counterpart, supporting the reality of the SCUBA-2 detection. The inconsistency between the dust seen by SCUBA-2 and the radio emission may be explained by the 1-σ positional uncertainty of the data. The radio source is also coincident with a strong X-ray counterpart (Geach et al. 2009).

3.4.11. *LAB16*

The radio emission is detected around the center of the LAB and SCUBA-2 shows dust emission that peaks around 5 arcsec from the center, which is well within the 1-σ positional uncertainty of the data.

3.4.12. *LAB18*

This is the strongest submm source among all LABs in this field. The SCUBA-2 observations reveal a flux density of 5.4±0.9 mJy. The ALMA observations discover four dust cores (a, b, c, and d in right bottom panel of Figure 4) with a total flux density of 9.47±0.36 mJy, which is about 75% higher than the SCUBA-2 value. Three out of four ALMA submm sources have radio counterparts. ALMA-LAB18a peaks around the center of the LAB and ALMA-LAB18b lies south of the center with an offset of 4.5 arcsec. The latter is surrounded by Lyα emission. If the Lyα emission in the south is a part of LAB18, its elongation along the north-south direction is around 13 arcsec, i.e., 100 kpc. The other two submm sources, ALMA-LAB18c and ALMA-LAB18d, located farther to the south are outside the LAB and not associated with it. Geach et al. (2009) found an X-ray counterpart between two ALMA sources, ALMA-LAB18b and ALMA-LAB18c. However, the positional errors of the X-ray sources are expected to be the order of 2.5 arcsec in most cases (Lehmer et al. 2009). However, LAB18 is at the edge of the X-ray image. Therefore, its positional error will be even larger, and the X-ray source might be associated with either ALMA-LAB18b or ALMA-LAB18c.

3.4.13. *LAB30*

There are four radio sources detected in this region (Figure 3). The sources, A, C and D, show detections of high significance but are located outside of this LAB. Source D is found to be associated with a local galaxy at z=0.41 (Saez et al. 2015). Source B is close to the center of the LAB, but only marginally detected at 3σ. No submm emission is detected and the marginal detection of source B needs to be confirmed. We consider this source as undetected at radio wavelengths.

4. DISCUSSION

4.1. *Physical sizes of LABs and detection of submm/radio emission*

Figure 5 shows the distribution of Lyα luminosity, isophotal area and measured fluxes at submm wavelengths for all LABs. In the left panel, we plot the submm flux density against the Lyα luminosity. For the sources with $L_{\rm Ly\alpha}$>10^{43} ergs s^{-1}, 6 out of 17 LABs are detected at submm wavelengths. For the fainter sources with $L_{\rm Ly\alpha}$<10^{43} ergs s^{-1}, 3 out of 18 LABs are detected at submm wavelengths. Apparently, more Lyα luminous galaxies are more likely to be detected at submm wavelengths. In the right panel, we plot the submm flux density against the isophotal area. For the first 18 large LABs, which are named according to their isophotal area in Matsuda et al. (2004), 11 are detected in the submm. The remaining 17 LABs are not detected at submm wavelengths. This suggests that large LABs exhibit more strong submm/radio emission. Furthermore, our results suggest that the detection of submm dust emission in LABs is more linked to the physical sizes of Lyα emission than the Lyα luminosities of LABs. A recent study (Matsuda et al. 2012) shows that the spatial extent of the Lyα haloes is determined by the surrounding Mpc-scale environment, rather than by the central UV luminosities. This is inconsistent with the result in Xue et al. (2017), who don't find any correlation between measured scale-lengths and overdensity parameter. Of course, the smaller LABs may contain less massive SMGs. Therefore, our results may indicate that more massive galaxies tend to be formed in the LABs with large Lyα spatial extents that are visible at submm wavelengths. This also suggests that most massive galaxies tend to reside in the centers of protoclusters.

4.2. *Powering sources of LABs: star formation or active galactic nuclei?*

4.2.1. *Submm and radio detections in LABs and their implications to heating mechanisms*

The heating mechanism of LABs is still unclear. About one third of the LABs in SSA22 are associated with submm/radio sources with SFRs above 100 $M_\odot$/yr. Spectroscopic measurements from the literature (see Table 2) confirm that at least some of the detected submm/radio counterparts are indeed associated with the LABs. These results suggest that internal heating in the host galaxies may be a major energy source for some LABs, which is consistent with our recent study of J2143−4423 (Ao et al. 2015).

Alternately, AGN may also be responsible for heating the gas. Indeed, the deep *Chandra* X-ray observations in the SSA 22 field (Geach et al. 2009; Lehmer et al. 2009) find that 6 out of 29 LABs have X-ray counterparts, implying a significant fraction of AGN in LABs. Among these 6 X-ray detected LABs, LAB3 shows no counterparts at radio and submm wavelengths (for details see § 3.4 and Figure 3) and LAB18 is not clearly associated with any submm/radio counterparts, given the pointing accuracy of the *Chandra* observations (for details see § 3.4 and Figures 3 and 4). The remaining four LABs, LAB2, LAB12 and LAB14 identified in Geach et al. (2009), as well as LAB1 with weak X-ray emission (see Figure 4), are detected at radio and submm wavelengths. In the left panel of Figure 6, we plot $\rm SFR_{radio}$ against $\rm SFR_{submm}$. The detection limit set by the sensitivity of VLA observations is roughly shown as the solid horizontal line. If the submm/radio emission is purely produced by SF, the radio and FIR derived SFRs should be similar, as shown by the short-dashed line. All sources are well above it. This may be due to an overestimated $\rm SFR_{radio}$. If we multiply the $\rm SFR_{submm}$ by a factor of two, close to the maximum SFRs calculated from the adopted templates in § 3.3 and shown as the dashed line, two sources are below but most are still above it. This cannot be explained by the calibration methods of SFRs, and may be caused by the existence of AGN that provide an additional radio flux contribution in some cases. To clearly show the effect of AGN, we plot $\rm SFR_{radio}/SFR_{submm}$ ratios against $\rm SFR_{submm}$ in the right panel of Figure 6, suggesting that the radio excess is obviously driven by the AGN in some cases. It is clear that X-ray detected LABs have $\rm SFR_{radio}/SFR_{submm}$ ratios above 2.5. For the sources detected at both submm and radio wavelengths, 8 out of 10 LABs have ratios larger than 2.5, suggesting a relative radio excess in LABs is common. Previously taken radio/FIR data from local AGN (Rush et al. 1993,1996) show that Seyfert galaxies have a 3 times stronger 6cm radio continuum than predicted by star formation alone, indicating that the existence of AGN in submm/radio detected LABs might be common. This is consistent with the finding that 10 out of 12 LAEs with $L_{\rm Ly\alpha}$>10^{43} ergs s^{-1} are detected in X-rays with *Chandra* (Civano et al. 2016; Sorbral et al. 2017). However, it is very difficult to discriminate between predominately SF or AGN powered LABs. At least for the submm/radio-detected sources with SFRs larger than 100 $M_\odot$/yr, it is very likely that SF is an important heating mechanism, and among most of them AGN may also play an important role in powering the Lyα emission.

Note that the upper SFR limits of the submm-undetected sources by the SCUBA-2 measurements are about 200$M_\odot$/yr, which is usually much higher than the SFR determined by the Lyα luminosity. Therefore, it is diffi-

cult to draw a strong conclusion on the powering sources of these LABs with the current data, due to large variance of Lyα escape fraction (see § 4.3). Future deep observations are required to settle this problem.

4.2.2. *Locations of radio and X-ray counterparts within LABs and their implications to heating mechanisms*

Due to the limited angular resolution and positional uncertainties of the SCUBA-2 observations, it is impossible to pinpoint the accurate positions of the SMGs in the LABs with SCUBA-2 data alone. With the high angular resolution VLA images, the accurate positions of radio counterparts and their associated SMGs are now well determined. Among the sources with radio counterparts detected above 4σ, four LABs, LAB4, LAB5, LAB9 and LAB16, have no X-ray counterparts. It is very striking that except for LAB9 the remaining three sources are located in the center of the LABs. This may provide evidence in support of SF as the main powering source in these LABs, and is consistent with the SF-based model (e.g., Zheng et al. 2011) for LAB formation and recent observations by Matsuda et al. (2012) who find that stacking of fainter LAEs in the SSA 22 field shows the extended and faint Lyα emission surrounding the bright sources at the center. However, the existence of AGN in these LABs can not be excluded. Especially, LAB4 has a high $\mathrm{SFR_{radio}/SFR_{submm}}$ ratio of 5.1, strongly supporting that an AGN may reside there. Thus, these sources without X-ray emission may also host AGNs, but still deeply embedded in their host galaxies where X-ray emission might be efficiently absorbed. This is supported by the fact that these four LABs are the most massive ones among all LABs.

X-ray emission has been detected toward 6 of the 29 LABs in the SSA22 field, including LAB1 with X-ray emission but not discussed in Geach et al. (2009), suggesting the existence of AGN in these systems. None of the X-ray sources is located at the LAB's center. This might be explained if the X-ray sources are always associated with merging systems which re-distribute the interstellar meidium (ISM) and circumgalactic medium (CGM) into inhomogeneous morphology. Deep near IR imaging (Uchimoto et al. 2012) shows that 3 out of 5 X-ray detected LABs contain multiple counterparts, suggesting there are merging systems in these LABs. The Lyα emission is mainly resonantly scattered by neutral hydrogen atoms in the ISM and CGM, and therefore its distribution may reflect the inhomogeneous morphology of ISM and CGM regulated by the merging systems. Alternatively, it is very likely that all LABs contain AGNs, as described in § 4.2.1. Compared to four LABs without X-ray emission, these X-ray detected sources are less massive. Massive ones are still deeply embedded due to high dust obscuration, and less massive ones provide strong feedbacks, which play an important role in heating surrounding gas and making Lyα emission more extended and inhomogeneous.

4.3. *Lyα escape fraction at z=3.1*

It is very interesting to know the Lyα escape fraction, $f_{\rm esc}^{\rm Ly\alpha}$, in LABs, a special class of LAEs, and to understand it in different environments. Traditionally, the Lyα escape fraction at $z\geq$2.3 is mainly derived from the Lyα and UV/Hα luminosity function (e.g., Hayes et al. 2011a; Sobral et al. 2017). Dust emission is directly related to the SF activity in galaxies and has been widely used as a good SFR estimator (Kennicutt 1998; Kennicutt & Evans 2012). Therefore, using SCUBA-2/ALMA data, the Lyα escape fraction can also be calculated from the ratio of Lyα to dust continuum derived SFRs. In Figure 7, we plot $f_{\rm esc}^{\rm Ly\alpha}$ against the SFRs and Lyα luminosities of the LABs. In our sample, the median Lyα escape fraction for the submm-detected LABs is about 3%. Except for 11 submm-detected sources, the remaining LABs not detected at submm wavelengths can also provide important constraints on $f_{\rm esc}^{\rm Ly\alpha}$. Lower limits of $f_{\rm esc}^{\rm Ly\alpha}$ can be estimated by using the upper limits of SCUBA-2 measurements and these values are presented in Figure 7. The median value of these lower limits is $\sim$2.5%. The Lyα escape fraction in the LABs is slightly lower but still comparable to the global Lyα escape fraction in the previous studies (Gronwall et al. 2007; Ouchi et al. 2008; Hayes et al. 2011a; Sobral et al. 2017). However, the fractions in the LAEs are usually much higher than the global values, as the LAEs are a biased sample, selected by their strong Lyα emission. Indeed, Hayes et al. (2010) reported $f_{\rm esc}^{\rm Ly\alpha} > 32\%$ for LAEs at z=2.2, Sobral et al. (2017) shows that $f_{\rm esc}^{\rm Ly\alpha}$ is around 37% for LAEs at z=2.23, and Wardlow et al. (2014) use far-infrared data instead of optical data and obtain a lower limit of $f_{\rm esc}^{\rm Ly\alpha}$ to be 10 to 20% for LAEs at z=3.1.

To investigate the low Lyα escape fractions in the LABs, we compare our results with those of Hayes et al. (2010), Wardlow et al. (2014) and Sobral et al (2017). The measurements from these studies are also presented in Figure 7. It is obvious that at least for two third of the LABs, the measured $f_{\rm esc}^{\rm Ly\alpha}$ is mainly limited by the threshold of SCUBA-2 measurements, as shown by the dashed line in the right panel of Figure 7. The higher fraction from these submm-undetected LABs will widen the range of the Lyα escape fraction from the LABs. Thus, the low fraction from the submm-detected LABs only represents a minority of the whole sample. We find a big difference between our sample and those of Hayes et al. (2010), Wardlow et al. (2014) and Sobral et al (2017) that the SFRs of the submm-detected LABs

are much higher than those in the latter three samples. The galaxies with high SFRs are most likely massive galaxies with a large amount of dust in the systems. We suspect that the low Lyα escape fractions in the submm-detected LABs are probably due to high dust attenuation as their SFRs are about one magnitude higher than the samples in other studies. Another reason may be related to the large-scale environment around the LABs. All sources are located in the dense region of SSA 22, which contains a large amount of circumgalactic medium. In such an environment, Lyα photons experience numerous resonance scatterings, and can also be easily absorbed by dust, making the Lyα emission more extended and leading to a lower escape fraction. This is consistent with the recent study of Shimakawa et al. (2017) who find that Lyα escape fractions in high-density regions are lower than in low-density regions. We also note that three LABs, LAB1, LAB2 and LAB3, have similar Lyα escape fractions as the LAEs studied by Hayes et al. (2010), Wardlow et al. (2014) and Sobral et al (2017). All these sources have X-ray emission. Their high fractions may be partially due to the AGN in the host galaxies. The AGN will produce additional photons and feedback to possibly remove the material surrounding the centers and then enhance the Lyα emission by increasing the escaping photons from the central regions. To better understand the physical origin of the low Lyα escape fraction in the LABs, deep submm observations will be useful.

5. CONCLUSIONS

We have presented submm data from JCMT/SCUBA-2 observations together with ALMA data towards 35 LABs identified in the SSA22 field by Matsuda et al. (2004) and deep radio images with the VLA towards 29 out of the 35 LABs. We also discuss the deep X-ray data from the same region. Our conclusions are as follows.

1. With the JCMT/SCUBA-2 and ALMA, 11 out of 35 LABs show dust emission. With the VLA, 9 out of 29 LABs are detected at radio wavelengths. For 5 out of the 9 radio detected sources, spectroscopic data from the literature reveal redshifts around 3.1, confirming that the radio counterparts and the corresponding submm sources are associated with the LABs.

2. The detection of submm dust emission in LABs is more linked to the physical sizes of Lyα emission than the Lyα luminosities of LABs. The results indicate that more massive galaxies tend to be formed in the LABs with large Lyα spatial extents, and also suggests that most massive galaxies tend to reside in the centers of protoclusters.

3. The 11 LABs detected at submm wavelengths have SFRs over 100 $M_{\odot}$/yr, favoring star formation as the major energy source for some LABs. Our results show that a radio excess is common in the submm/radio detected LABs and therefore AGN may also play an important role to power the Lyα emission.

4. Among the four radio detected LABs lacking X-ray emission, three sources are located in the center of their parent LABs. However, all X-ray sources are not located at the center of their associated LABs. This may be explained if the X-ray sources are always associated with merging systems, which re-distribute the intergalactic medium and create an inhomogeneous morphology. Alternatively, AGN and its feedback may be responsible for the inhomogeneous Lyα morphology.

5. The escape fraction of Lyα photons in the LABs are significantly lower than those in the LAEs in other studies. We suspect that this large difference is due to the SCUBA-2 detection threshold, the high dust attenuation supported by the large SFRs in our sample as well as the dense large-scale environment in SSA22.

Y.A. acknowledges partial support by NSFC grant 11373007 and Youth Innovation Promotion Association CAS. M.H. acknowledges the support of the Swedish Research Council, Vetenskapsrådet and the Swedish National Space Board (SNSB), and is Fellow of the Knut and Alice Wallenberg Foundation. N.K.H. is supported by the Science and Technology Facilities Council (grant number ST/K502029/1).

The James Clerk Maxwell Telescope has historically been operated by the Joint Astronomy Centre on behalf of the Science and Technology Facilities Council of the United Kingdom, the National Research Council of Canada and the Netherlands Organisation for Scientific Research. Additional funds for the construction of SCUBA-2 were provided by the Canada Foundation for Innovation. The James Clerk Maxwell Telescope is operated by the East Asian Observatory on behalf of The National Astronomical Observatory of Japan, Academia Sinica Institute of Astronomy and Astrophysics, the Korea Astronomy and Space Science Institute, the National Astronomical Observatories of China

and the Chinese Academy of Sciences (Grant No. XDB09000000), with additional funding support from the Science and Technology Facilities Council of the United Kingdom and participating universities in the United Kingdom and Canada.

This paper makes use of the following ALMA data: ADS/JAO.ALMA#2013.1.00162.S and ADS/JAO.ALMA#2013.1.00704.S. ALMA is a partnership of ESO (representing its member states), NSF (USA) and NINS (Japan), together with NRC (Canada), NSC and ASIAA (Taiwan), and KASI (Republic of Korea), in cooperation with the Republic of Chile. The Joint ALMA Observatory is operated by ESO, AUI/NRAO and NAOJ.

REFERENCES

Alexander, D. M., Simpson, J. M., Harrison, C. M., et al. 2016, MNRAS, 461, 2944

Ao, Y., Matsuda, Y., Beelen, A., et al. 2015, A&A, 581, A132

Bell, E. F. 2003, ApJ, 586, 794

Bridge, C. R., Blain, A., Borys, C. J. K., et al. 2013, ApJ, 769, 91

Cen, R., & Zheng, Z. 2013, ApJ, 775, 112

Chapin, E. L., Berry, D. S., Gibb, A. G., et al. 2013, MNRAS, 430, 2545

Civano, F., Marchesi, S., Comastri, A., et al. 2016, ApJ, 819, 62

Colbert, J. W., Teplitz, H., Francis, P., et al. 2006, ApJL, 637, L89

Condon, J. J., Cotton, W. D., Fomalont, E. B., et al. 2012, ApJ, 758, 23

Condon, J. J., Cotton, W. D., Greisen, E. W., et al. 1998, AJ, 115, 1693

Dekel, A., Birnboim, Y., Engel, G., et al. 2009, Nature, 457, 451

Dey, A., Bian, C., Soifer, B. T., et al. 2005, ApJ, 629, 654

Dijkstra, M., & Loeb, A. 2009, MNRAS, 400, 1109

Erb, D. K., Bogosavljević, M., & Steidel, C. C. 2011, ApJL, 740, L31

Faucher-Giguère, C.-A., Kereš, D., Dijkstra, M., Hernquist, L., & Zaldarriaga, M. 2010, ApJ, 725, 633

Francis, P. J., Woodgate, B. E., Warren, S. J., et al. 1996, ApJ, 457, 490

Furlanetto, S. R., Schaye, J., Springel, V., & Hernquist, L. 2005, ApJ, 622, 7

Geach, J. E., Alexander, D. M., Lehmer, B. D., et al. 2009, ApJ, 700, 1

Geach, J. E., Bower, R. G., Alexander, D. M., et al. 2014, ApJ, 793, 22

Geach, J. E., Dunlop, J. S., Halpern, M., et al. 2017, MNRAS, 465, 1789

Geach, J. E., Matsuda, Y., Smail, I., et al. 2005, MNRAS, 363, 1398

Geach, J. E., Narayanan, D., Matsuda, Y., et al. 2016, ApJ, 832, 37

Gronwall, C., Ciardullo, R., Hickey, T., et al. 2007, ApJ, 667, 79

Haiman, Z., Spaans, M., & Quataert, E. 2000, ApJL, 537, L5

Hayes, M. 2015, PASA, 32, e027

Hayes, M., Östlin, G., Schaerer, D., et al. 2010, Nature, 464, 562

Hayes, M., Scarlata, C., & Siana, B. 2011b, Nature, 476, 304

Hayes, M., Schaerer, D., Östlin, G., et al. 2011a, ApJ, 730, 8

Hine, N. K., Geach, J. E., Matsuda, Y., et al. 2016, MNRAS, 460, 4075

Holland, W. S., Bintley, D., Chapin, E. L., et al. 2013, MNRAS, 430, 2513

Ivison, R. J., Magnelli, B., Ibar, E., et al. 2010, A&A, 518, L31

Kennicutt, R. C., & Evans, N. J. 2012, ARA&A, 50, 531

Kennicutt, R. C., Jr. 1998, ARA&A, 36, 189

Kereš, D., Katz, N., Weinberg, D. H., & Davé, R. 2005, MNRAS, 363, 2

Kubo, M., Uchimoto, Y. K., Yamada, T., et al. 2013, ApJ, 778, 170

Kubo, M., Yamada, T., Ichikawa, T., et al. 2015, ApJ, 799, 38

Lehmer, B. D., Alexander, D. M., Chapman, S. C., et al. 2009, MNRAS, 400, 299

Matsuda, Y., Iono, D., Ohta, K., et al. 2007, ApJ, 667, 667

Matsuda, Y., Nakamura, Y., Morimoto, N., et al. 2009, MNRAS, 400, L66

Matsuda, Y., Yamada, T., Hayashino, T., et al. 2011, MNRAS, 410, L13

Matsuda, Y., Yamada, T., Hayashino, T., et al. 2012, MNRAS, 425, 878

Matsuda, Y., Yamada, T., Hayashino, T., et al. 2004, AJ, 128, 569

Mori, M., & Umemura, M. 2006, Nature, 440, 644

Nilsson, K. K., Fynbo, J. P. U., Møller, P., Sommer-Larsen, J., & Ledoux, C. 2006, A&A, 452, L23

Ouchi, M., Shimasaku, K., Akiyama, M., et al. 2008, ApJS, 176, 301-330

Overzier, R. A., Nesvadba, N. P. H., Dijkstra, M., et al. 2013, ApJ, 771, 89
Palunas, P., Teplitz, H. I., Francis, P. J., Williger, G. M., & Woodgate, B. E. 2004, ApJ, 602, 545
Prescott, M. K. M., Dey, A., Brodwin, M., et al. 2012b, ApJ, 752, 86
Prescott, M. K. M., Dey, A., & Jannuzi, B. T. 2013, ApJ, 762, 38
Prescott, M. K. M., Dey, A., & Jannuzi, B. T. 2012a, ApJ, 748, 125
Rush, B., Malkan, M. A., & Edelson, R. A. 1996, ApJ, 473, 130
Rush, B., Malkan, M. A., & Spinoglio, L. 1993, ApJS, 89, 1
Saez, C., Lehmer, B. D., Bauer, F. E., et al. 2015, MNRAS, 450, 2615
Saito, T., Shimasaku, K., Okamura, S., et al. 2006, ApJ, 648, 54
Shimakawa, R., Kodama, T., Hayashi, M., et al. 2017, MNRAS, 468, L21
Silva, L., Granato, G. L., Bressan, A., & Danese, L. 1998, ApJ, 509, 103
Smith, D. J. B., & Jarvis, M. J. 2007, MNRAS, 378, L49
Sobral, D., Matthee, J., Best, P., et al. 2017, MNRAS, 466, 1242
Steidel, C. C., Adelberger, K. L., Shapley, A. E., et al. 2003, ApJ, 592, 728
Steidel, C. C., Adelberger, K. L., Shapley, A. E., et al. 2000, ApJ, 532, 170
Swinbank, A. M., Simpson, J. M., Smail, I., et al. 2014, MNRAS, 438, 1267
Swinbank, A. M., Smail, I., Longmore, S., et al. 2010, Nature, 464, 733
Tamura, Y., Matsuda, Y., Ikarashi, S., et al. 2013, MNRAS, 430, 2768
Tamura, Y., Kohno, K., Nakanishi, K., et al. 2009, Nature, 459, 61
Taniguchi, Y., & Shioya, Y. 2000, ApJL, 532, L13
Uchimoto, Y. K., Yamada, T., Kajisawa, M., et al. 2012, ApJ, 750, 116
Umehata, H., Tamura, Y., Kohno, K., et al. 2014, MNRAS, 440, 3462
Umehata, H., Tamura, Y., Kohno, K., et al. 2015, ApJL, 815, L8
Umehata, H., Matsuda, Y., Tamura, Y., et al. 2017a, ApJL, 834, L16
Umehata, H., Tamura, Y., Kohno, K., et al. 2017b, ApJ, 835, 98
Wardlow, J. L., Malhotra, S., Zheng, Z., et al. 2014, ApJ, 787, 9
Webb, T. M. A., Yamada, T., Huang, J.-S., et al. 2009, ApJ, 692, 1561
Wilman, R. J., Gerssen, J., Bower, R. G., et al. 2005, Nature, 436, 227
Xue, R., Lee, K.-S., Dey, A., et al. 2017, ApJ, 837, 172
Yajima, H., Li, Y., & Zhu, Q. 2013, ApJ, 773, 151
Yamada, T., Matsuda, Y., Kousai, K., et al. 2012, ApJ, 751, 29
Yang, Y., Decarli, R., Dannerbauer, H., et al. 2012, ApJ, 744, 178
Yang, Y., Zabludoff, A., Eisenstein, D., & Davé, R. 2010, ApJ, 719, 1654
Yang, Y., Zabludoff, A., Tremonti, C., Eisenstein, D., & Davé, R. 2009, ApJ, 693, 1579
Zheng, Z., Cen, R., Weinberg, D., Trac, H., & Miralda-Escudé, J. 2011, ApJ, 739, 62

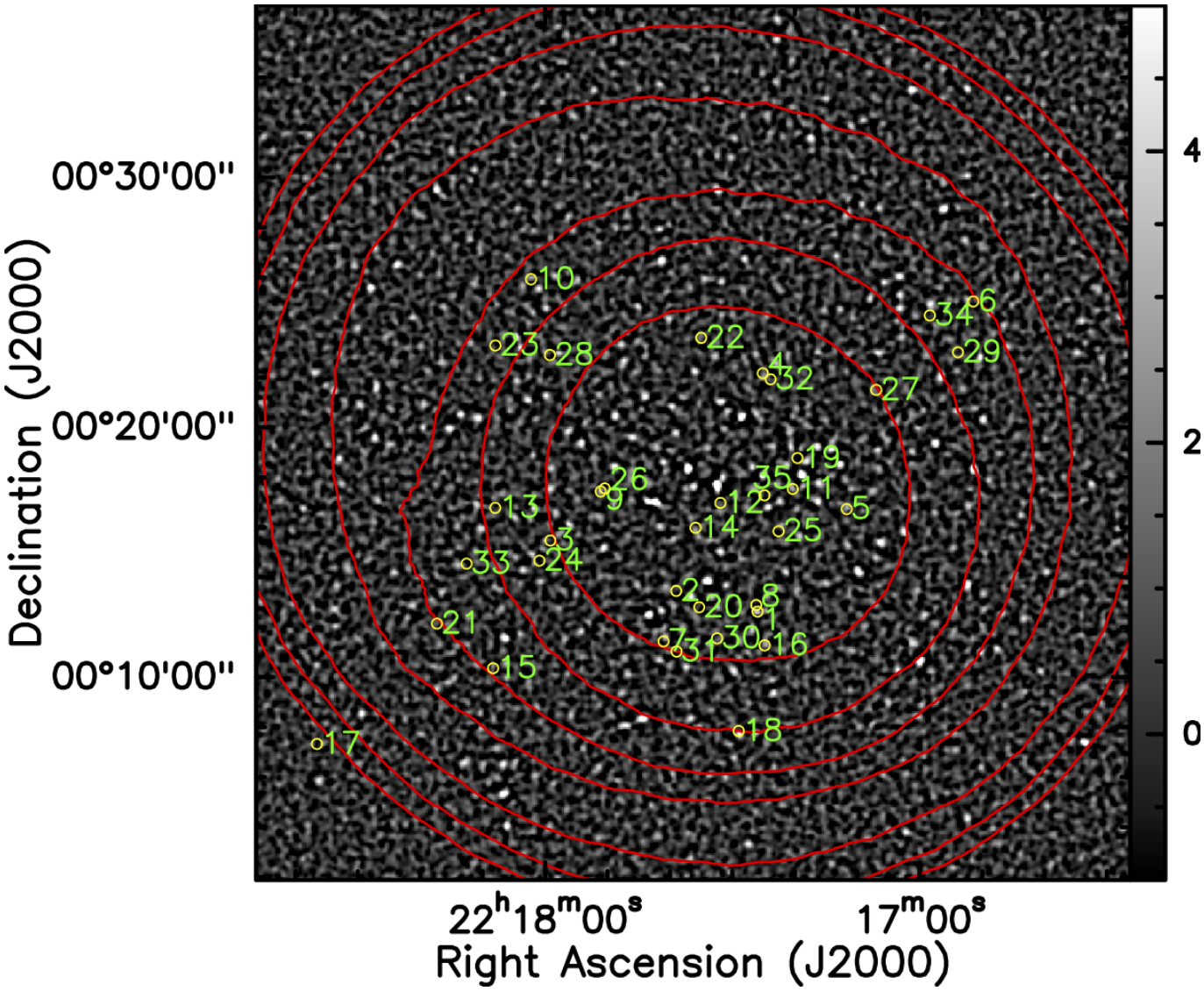

Figure 1. The noise map of the SCUBA-2 data with contour levels of 0.8, 0.9, 1.0, 1.1, 1.3, 1.5 and 1.7 mJy/beam overlaied on a signal-to-noise map in a grey image. The locations of the 35 LABs identified by Matsuda et al. (2004) are shown as yellow circles with diameters of 25 arcsec. The ID numbers of the sources are indicated in green.

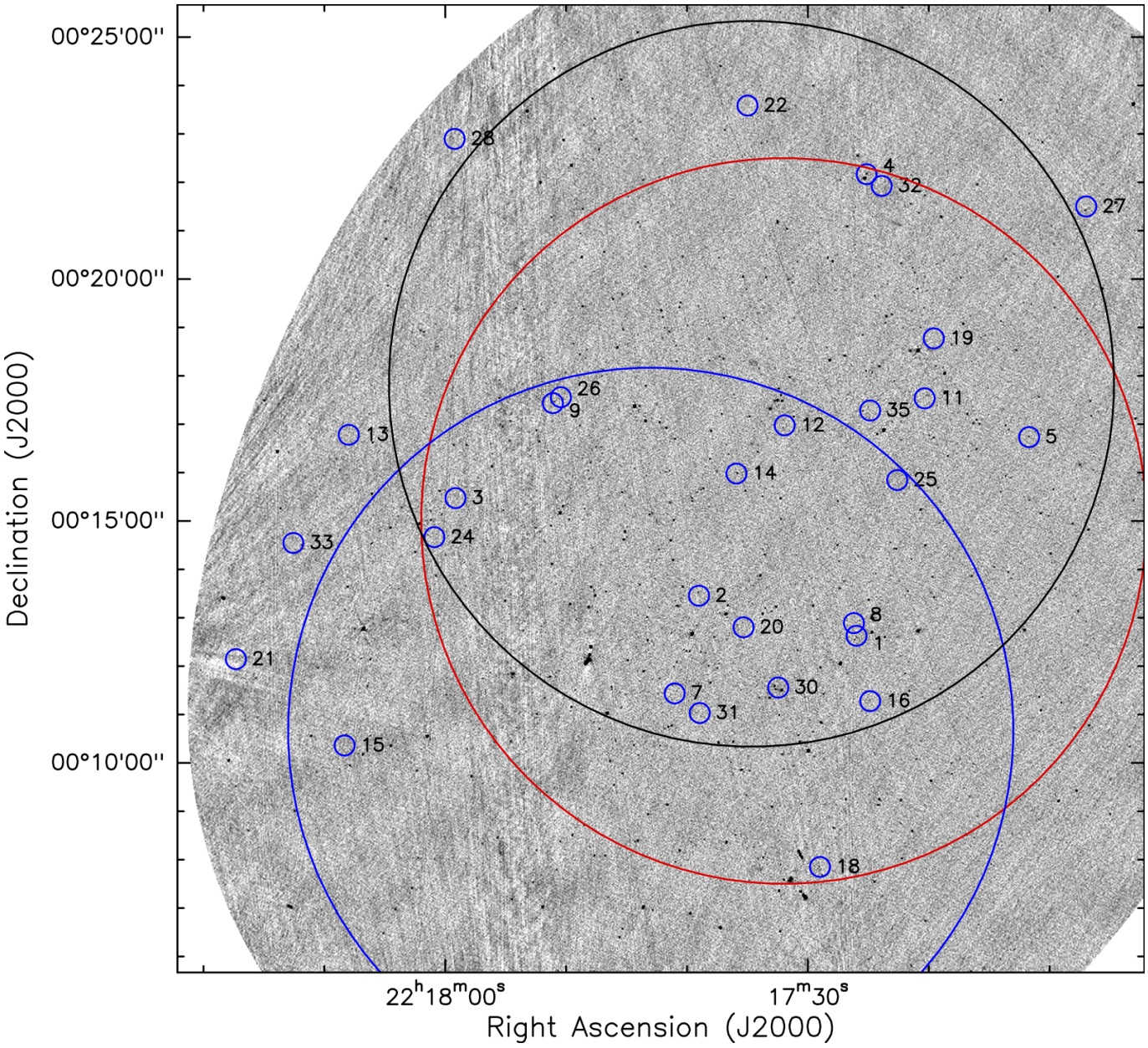

Figure 2. A radio map of the SSA22 region in grey scale. Three big circles denote the primary full width to half maximum beam size for three pointings with different on-source observing time (red: 26 hours, blue: 1.6 hours and green: 4.2 hours). The locations of 29 out of the 35 LABs identified by Matsuda et al. (2004) are covered by our observations and are shown as blue circles with diameters of 25 arcsec. The ID numbers of the sources are labelled in black.

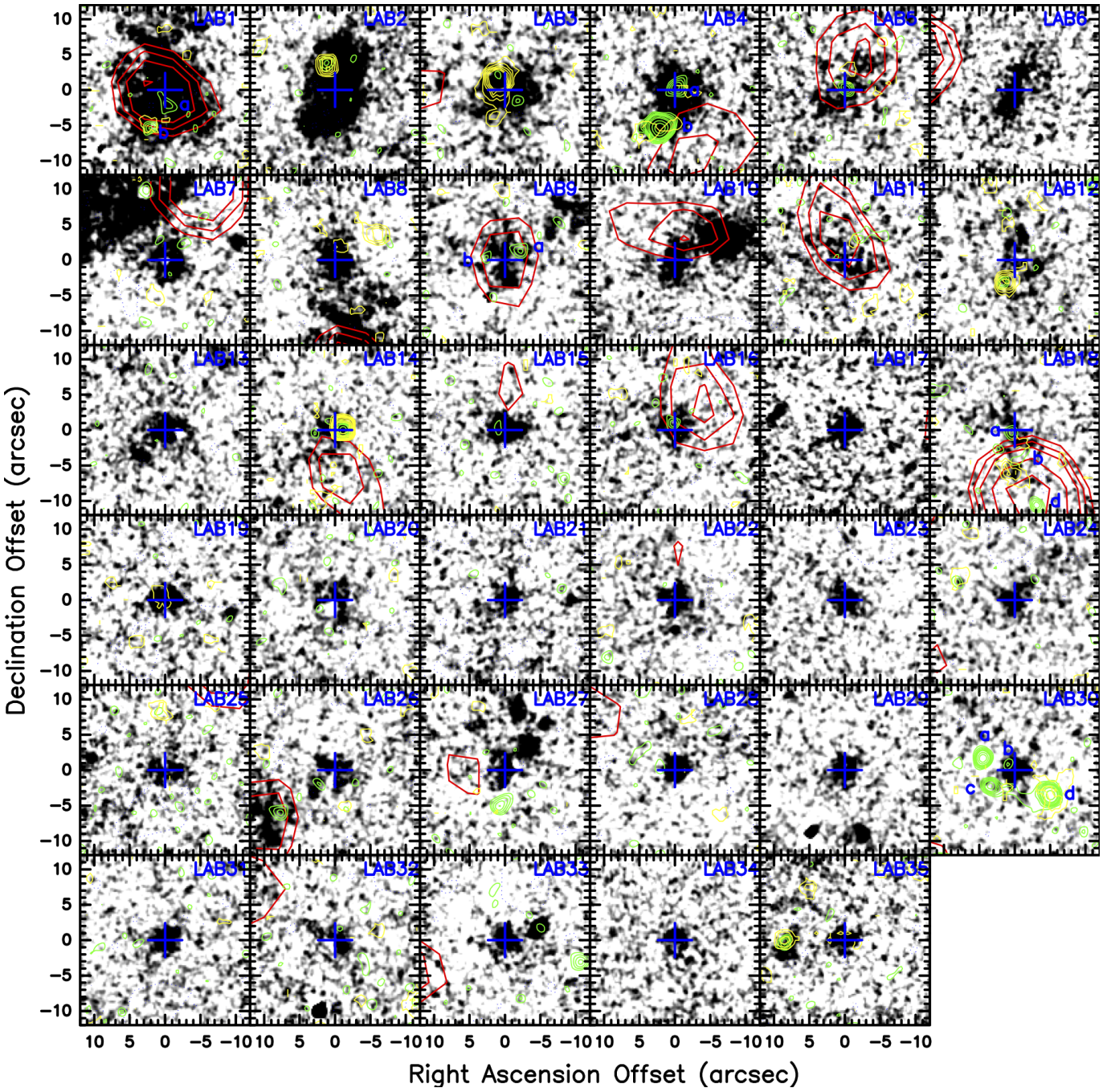

Figure 3. SCUBA2 dust emission at 850 μm in red (the contour levels are -2, 2, 2.5, 3, 4 and 5 times the respective noise level, the latter given in Column 4 of Table 2), VLA radio emission at 3 GHz in green (contour levels are -2, 2, 3, 4, 5, 6, 8, 10, 15, 20 and 30σ and the values of σ are the noise levels prior to primary beam correction given in Column 6 of Table 2) and *Chandra* X-ray emission in yellow (the contour levels of number counts of the smoothed full-band, 0.5-8 keV, image adopted from Lehmer et al. 2009 are 6, 9, 12, 15, 18, 21, 30, 40 and 50) are overlaid on the Lyα emission taken from Matsuda et al. (2004). Radio sources are labelled with letters in blue when more than one radio cores are detected in one LAB. The offsets are relative to the centers of the LABs, denoted by blue crosses.

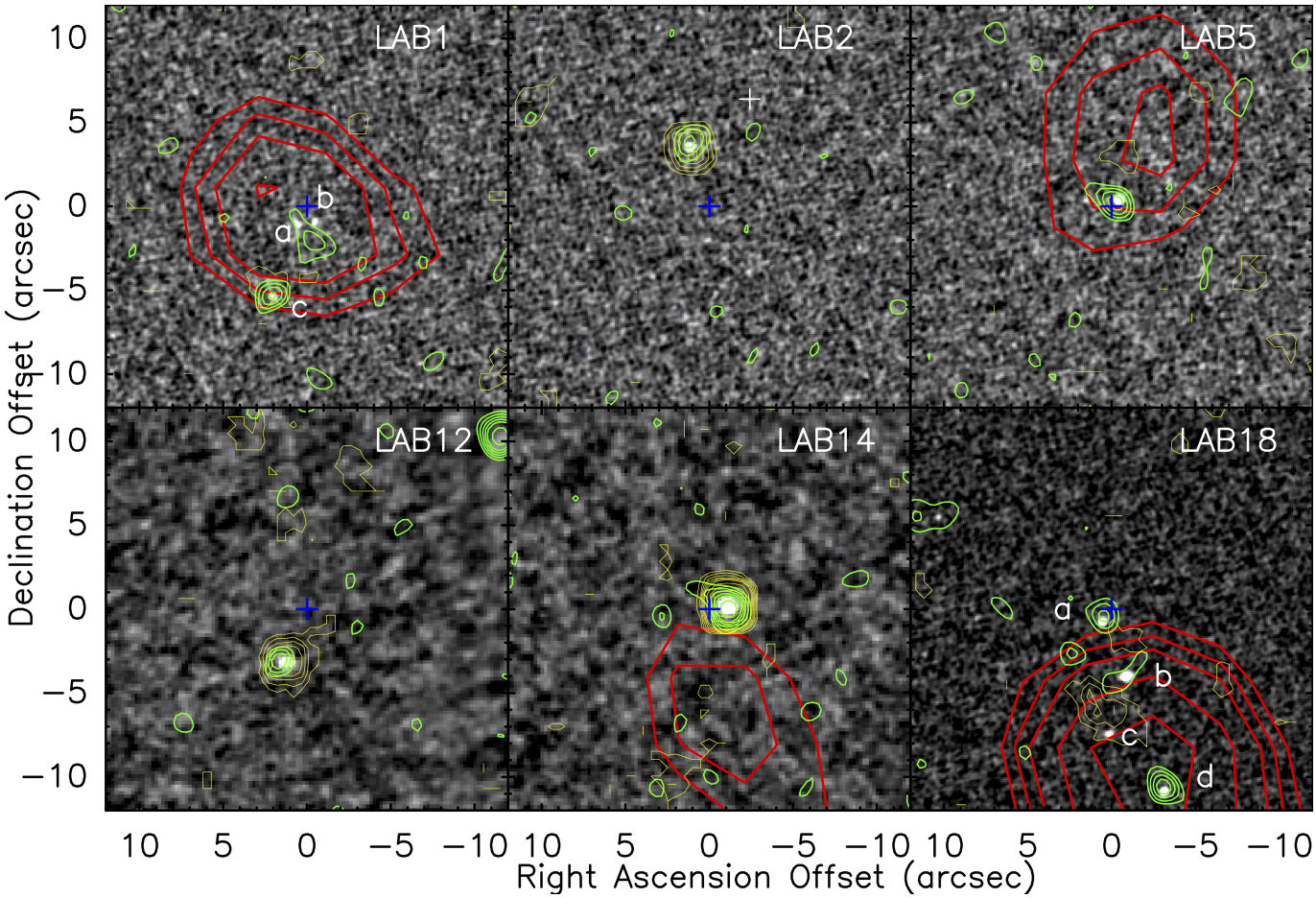

Figure 4. SCUBA2 dust emission at 850 μm (red), VLA radio emission at 3 GHz (green) and *Chandra* X-ray emission (yellow) contours are overlaid on the continuum images (LAB12 and LAB14 at 1.14mm and others at 850 μm) of the LABs observed with ALMA. The offsets are relative to the centers of the LABs. The contour levels are the same as in Figure 3. ALMA dust continuum sources are labelled with letters in white when more than one dust cores are detected in LABs. The white cross in the panel of LAB2 denotes the location of dust continuum marginally detected at 870 μm by Alexander et al. (2016)

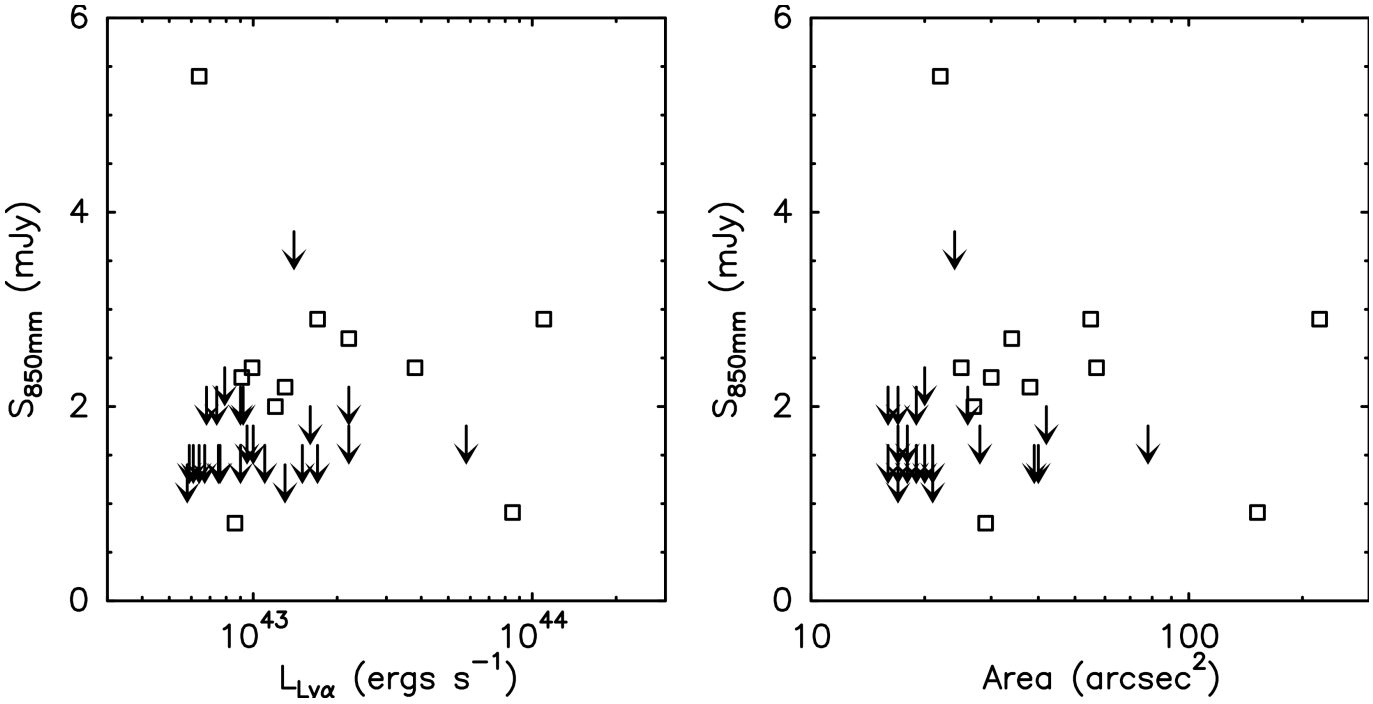

Figure 5. Distribution of measured 850μm flux versus Lyα luminosity (left panel) and isophotal area (right panel) for the LABs in the SSA22 field. The squares denote the LABs detected at 850μm and the arrows mark undetected sources.

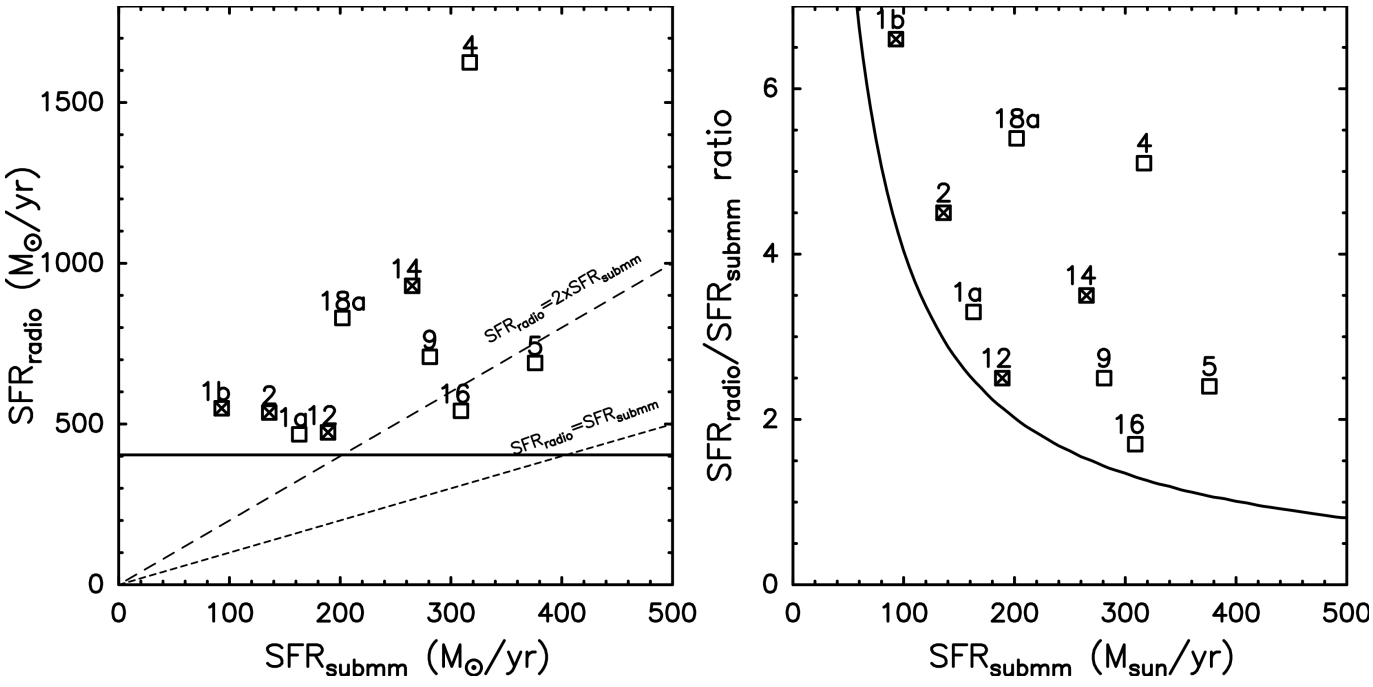

Figure 6. SFR_{radio}/SFR_{submm} ratios for the LABs detected at dust and radio wavelengths. The sources detected in X-rays are shown with cross symbols inside the squares. The solid lines present the detection limit, corresponding to a radio flux of 6.3 μJy, constrained by the VLA observations. The short-dashed and long-dashed lines denote $SFR_{radio}/SFR_{submm} = 1$ and 2, respectively.

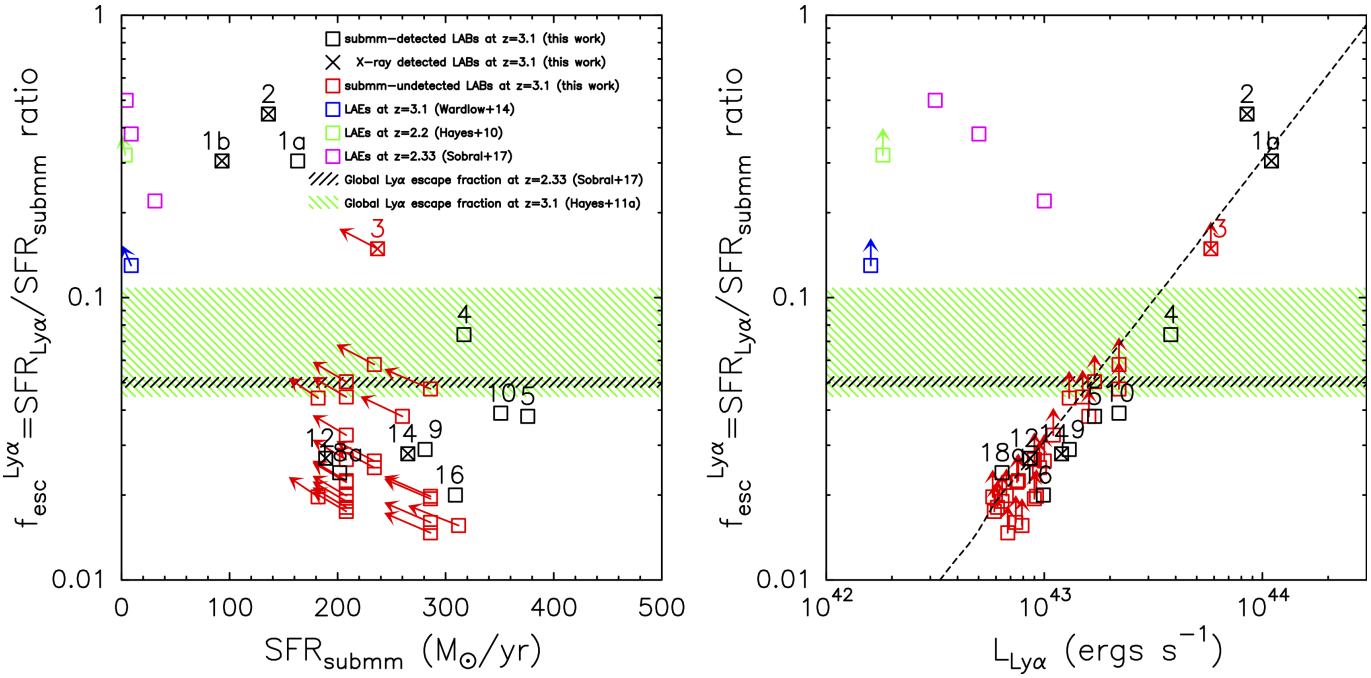
submm−detected LABs at z=3.1 (this work)
X−ray detected LABs at z=3.1 (this work)
submm−undetected LABs at z=3.1 (this work)
LAEs at z=3.1 (Wardlow+14)
LAEs at z=2.2 (Hayes+10)
LAEs at z=2.33 (Sobral+17)
Global Lyα escape fraction at z=2.33 (Sobral+17)
Global Lyα escape fraction at z=3.1 (Hayes+11a)
f_esc^Lyα=SFR_Lyα/SFR_submm ratio
SFR_submm (M⊙/yr)
L_Lyα (ergs s^−1)

Figure 7. Plots of escape fraction, $f_{\rm esc}^{\rm Ly\alpha}$, against star formation rate (**left**) and Lyα luminosity (**right**). Submm-detected and submm-undetected LABs are marked by black and red squares, respectively. X-ray detected LABs are indicated by crosses inside the squares. Lower limits of $f_{\rm esc}^{\rm Ly\alpha}$ for LAEs at $z=2.2$ and 3.1 are presented in green (Hayes et al. 2010) and blue (Wardlow et al. 2014), respectively. The fractions for LAEs at $z=2.23$ in Sobral et al. (2017) are shown in magenta. The global Lyα escape fractions at $z=2.33$ (Sobral et al. 2017) and $z=3.1$ (Hayes et al. 2011a) are denoted by black and green hashed regions, respectively. The dashed line in the right panel denotes the lower limit of $f_{\rm esc}^{\rm Ly\alpha}$ constrained by the SCUBA-2 detection threshold of 200 $M_\odot$/yr. Some detected sources above this line are due to better sensitivities of the ALMA measurements. Some undetected LABs well below the line are limited by their poor sensitivities outside the central field of the SCUBA-2 observations.

Table 1. Observation logs in SSA22

Telescope	Observation date	Project	RA (J2000)	Dec. (J2000)	Freq. (GHz)	Map size[a] (arcmin)	Observing time (hours)	On-source time (hours)
JCMT/SCUBA-2	2012.09 to 2013.12	MJLSC02	22:17:36.30	+00:19:22.7	345	30	...	72
JCMT/SCUBA-2	2015.04 to 2015.06	M15AI91	22:17:31.70	+00:17:50.0	345	15	...	19
VLA	2015.04 to 2015.04	15A-120	22:17:28.00	+00:17:50.0	2−4	15	6.7	4.2
VLA	2016.05 to 2016.05	16A-310	22:17:43.00	+00:10:40.0	2−4	15	2	1.6
VLA	2016.05 to 2016.08	16A-310	22:17:32.00	+00:15:00.0	2−4	15	32	26.1

[a] The map size of the VLA observations is the Field of View at the central frequency of 3 GHz.

Note that the best sensitivities in the images are 0.75 mJy/beam for the combined SCUBA-2 observations and 1.5 μJy/beam for the combined VLA observations, respectively.

Table 2. JCMT/SCUBA-2 and VLA S-band observations towards LABs in SSA22

				VLA observations[b]					Spectroscopic observations[c]			
Source	RA(J2000)	Dec(J2000)	$S_{850\mu m}$[a] (mJy)	VLA ID	rms (μJy)	offx ($''$)	offy ($''$)	S_{10cm} (μJy)	offx ($''$)	offy ($''$)	zred	ref
SCUBA2-LAB1	22:17:25.961	+00:12:37.57	**2.9±0.8**									
ALMA-LAB1ab	22:17:25.981	+00:12:36.35	**1.08±0.17**	**VLA-LAB1a**	1.64/1.79	-0.4	-1.1	7.3±2.2				
ALMA-LAB1c	22:17:26.100	+00:12:32.37	**0.64±0.12**	**VLA-LAB1b**	1.64/1.79	0.2	-0.1	8.6±2.2	0.0	-0.1	3.0993+/-0.0004	1
ALMA-LAB1			**1.72±0.21**									
SCUBA2-LAB2	22:17:38.996	+00:13:27.51	-0.5±0.8									
ALMA-LAB2	22:17:39.079	+00:13:30.85	**0.91±0.10**	**VLA-LAB2**	1.57/1.65	0.0	0.0	8.4±2.4	-0.5	-0.7	3.091+/-0.001	3
SCUBA2-LAB3	22:17:59.153	+00:15:28.37	0.2±0.9	VLA-LAB3	1.54/2.70	-1.9	-1.8	7.5±3.8				
SCUBA2-LAB4	22:17:25.126	+00:22:10.21	**2.4±0.8**	**VLA-LAB4a**	1.48/2.72	0.0	0.1	25.4±4.1				
				VLA-LAB4b	1.48/2.72	2.3	-5.6	98.9±3.8				
SCUBA2-LAB5	22:17:11.681	+00:16:43.95	**2.9±0.8**									
ALMA-LAB5	22:17:11.664	+00:16:44.32	**2.21±0.08**	**VLA-LAB5**	1.29/1.93	0.1	-0.4	10.8±2.7				
SCUBA2-LAB6	22:16:51.428	+00:25:02.39	0.4±1.0		n.a.							
SCUBA2-LAB7	22:17:41.005	+00:11:26.32	-1.0±0.8		1.52/1.81							
SCUBA2-LAB8	22:17:26.176	+00:12:53.53	-0.6±0.8		1.65/1.78							
SCUBA2-LAB9	22:17:51.084	+00:17:26.31	**2.2±0.8**	**VLA-LAB9a**	1.54/2.25	-2.0	0.7	11.1±3.4				
				VLA-LAB9b	1.54/2.25	2.6	0.0	7.0±3.4				
SCUBA2-LAB10	22:18:02.250	+00:25:55.77	**2.7±1.1**		n.a.							
SCUBA2-LAB11	22:17:20.325	+00:17:32.05	**2.3±0.7**	VLA-LAB11	1.46/1.78	-1.8	2.9	5.5±2.7				
SCUBA2-LAB12	22:17:31.907	+00:16:58.77	0.7±0.8									
ALMA-LAB12	22:17:32.01	+00:16:55.4	**0.7±0.1**	**VLA-LAB12**	1.61/1.70	0.2	0.1	7.4±2.4	-0.2	0.1	3.0909+/-0.0004	2
SCUBA2-LAB13	22:18:07.972	+00:16:46.77	0.1±0.9		1.32/3.95							
SCUBA2-LAB14	22:17:35.908	+00:15:58.79	**2.0±0.7**									
ALMA-LAB14	22:17:35.83	+00:15:59.0	**1.8±0.1**	**VLA-LAB14**	1.51/1.54	0.1	-0.4	14.5±2.1	1.0	0.0	3.094	4
SCUBA2-LAB15	22:18:08.317	+00:10:21.78	1.3±1.1		1.51/4.33							
SCUBA2-LAB16	22:17:24.845	+00:11:16.77	**2.4±0.8**	**VLA-LAB16**	1.44/1.77	0.2	0.6	8.5±2.7	0.8	0.7	3.0689+/-0.0002	2
SCUBA2-LAB17	22:18:36.533	+00:07:19.88	-1.5±1.9		n.a.							
SCUBA2-LAB18	22:17:28.998	+00:07:51.16	**5.4±0.9**									
ALMA-LAB18a	22:17:29.032	+00:07:50.26	**1.18±0.08**	**VLA-LAB18a**	1.58/2.80	-0.2	0.1	13.0±4.2				
ALMA-LAB18b	22:17:28.936	+00:07:46.92	**2.73±0.10**	VLA-LAB18b	1.58/2.80	-0.1	0.0	9.1±4.0				
ALMA-LAB18c	22:17:29.017	+00:07:43.44	**1.14±0.15**		1.58/2.80							
ALMA-LAB18d	22:17:28.781	+00:07:40.07	**4.42±0.30**	VLA-LAB18d	1.58/2.80	0.2	0.4	16.4±4.3				
ALMA-LAB18			**9.47±0.36**									

Table 2 continued on next page

Table 2 *(continued)*

				VLA observations[b]					Spectroscopic observations[c]			
Source	RA(J2000)	Dec(J2000)	$S_{850\mu m}$[a] (mJy)	VLA ID	rms (μJy)	offx ($''$)	offy ($''$)	S_{10cm} (μJy)	offx ($''$)	offy ($''$)	zred	ref
SCUBA2-LAB19	22:17:19.569	+00:18:46.38	-2.1±0.7		1.56/2.09							
SCUBA2-LAB20	22:17:35.307	+00:12:48.31	-0.4±0.8		1.60/1.68							
SCUBA2-LAB21	22:18:17.324	+00:12:08.66	1.1±1.2		1.63/6.63							
SCUBA2-LAB22	22:17:34.982	+00:23:35.09	1.5±0.8		1.31/3.45							
SCUBA2-LAB23	22:18:07.950	+00:23:16.62	-0.1±1.1		n.a.							
SCUBA2-LAB24	22:18:00.905	+00:14:40.10	-0.9±0.8		1.64/2.93							
SCUBA2-LAB25	22:17:22.590	+00:15:50.86	-2.1±0.8		1.43/1.57							
SCUBA2-LAB26	22:17:50.424	+00:17:33.37	0.6±0.8		1.50/2.17							
SCUBA2-LAB27	22:17:06.974	+00:21:30.15	1.7±0.8		1.29/3.70							
SCUBA2-LAB28	22:17:59.210	+00:22:53.96	-0.1±0.9		1.41/5.83							
SCUBA2-LAB29	22:16:53.869	+00:23:00.39	0.3±1.1		n.a.							
SCUBA2-LAB30	22:17:32.454	+00:11:33.36	0.6±0.9	VLA-LAB30a	1.72/1.91	4.6	1.6	24.9±2.4				
				VLA-LAB30b	1.72/1.91	1.1	0.7	4.3±2.4				
				VLA-LAB30c	1.72/1.91	3.4	-2.5	20.0±2.6				
				VLA-LAB30d	1.72/1.91	-4.8	-3.7	46.9±2.6				
SCUBA2-LAB31	22:17:38.945	+00:11:01.87	-0.7±0.8		1.48/1.78							
SCUBA2-LAB32	22:17:23.874	+00:21:55.46	0.6±0.7		1.50/2.75							
SCUBA2-LAB33	22:18:12.553	+00:14:32.67	-0.6±1.1		1.41/4.92							
SCUBA2-LAB34	22:16:58.365	+00:24:29.08	-0.7±1.1		n.a.							
SCUBA2-LAB35	22:17:24.837	+00:17:16.92	-0.3±0.8		1.58/1.77							

[a] The fluxes are measured at 850μm by JCMT/ALMA except for LAB12 and LAB14. The latter two sources were observed at 1.14mm with the ALMA. The sources detected at submm wavelengths are highlighted in bold font.

[b] In Column 6, the given two values are for the noise levels before and after primary beam correction. The offsets of radio counterparts relative to the LAB centers or ALMA sources are given in Column 7 & 8. The counterparts associated with the LABs are highlighted in bold font.

[c] Only the targets with offsets (Column 10 & 11) less than 1 arsec relative to the radio sources are considered to be associated with the radio sources. References: 1. Umehata et al. (2017b); 2. Kubo et al. (2015); 3. Steidel et al. (2003); 4. Yamada et al. (2012)

Table 3. Derived star formation rates towards submm/radio-detected LABs in SSA22

Source	$SFR_{850\mu m}$ [a] ($M_\odot$/yr)	Radio comp	SFR_{10cm} [a]	$SFR_{10cm}/SFR_{850\mu m}$ ($M_\odot$/yr)	$SFR_{Ly\alpha}$ [a] ($M_\odot$/yr)	$SFR_{Ly\alpha}/SFR_{850\mu m}$ (%)
SCUBA2-LAB1	376^{+332}_{-99}	VLA-LAB1	1017±198	2.7	68	18.1
ALMA-LAB1ab	140^{+124}_{-37}	VLA-LAB1a	468±140	3.3		
ALMA-LAB1c	83^{+73}_{-22}	VLA-LAB1b	549±140	4.6		
ALMA-LAB1	223^{+197}_{-59}	VLA-LAB1	1017±198	4.0	68	30.5
SCUBA2-LAB2	<195	VLA-LAB2	536±156	>2.7	52	>26.5
ALMA-LAB2	118^{+104}_{-31}	VLA-LAB2	536±156	4.5	52	44.7
SCUBA2-LAB3[b]	<237	...	<482	...	36	>14.9
SCUBA2-LAB4	317^{+280}_{-84}	VLA-LAB4a	1625±264	5.1	23	7.4
		VLA-LAB4b	6342±242			
SCUBA2-LAB5	382^{+338}_{-101}	VLA-LAB5	690±175	1.8	10	2.7
ALMA-LAB5	287^{+254}_{-76}	VLA-LAB5	690±175	2.4	10	3.8
SCUBA2-LAB9	281^{+248}_{-74}	VLA-LAB9a	709±215	2.5	8.0	2.9
		VLA-LAB9b	450±218			
SCUBA2-LAB10	349^{+308}_{-92}	...	...	...	14	3.9
SCUBA2-LAB11	302^{+266}_{-80}	VLA-LAB11	352±172	1.2	5.6	1.8
SCUBA2-LAB12	<214	VLA-LAB12	474±156	>2.2	5.3	>2.5
ALMA-LAB12	189^{+76}_{-19}	VLA-LAB12	474±156	2.5	5.3	2.7
SCUBA2-LAB14	265^{+234}_{-70}	VLA-LAB14	930±137	3.5	7.4	2.8
ALMA-LAB14	389^{+227}_{-63}	VLA-LAB14	930±137	2.4	7.4	1.9
SCUBA2-LAB16	309^{+273}_{-82}	VLA-LAB16	541±170	1.7	6.1	2.0
SCUBA2-LAB18	696^{+615}_{-184}	VLA-LAB18abd	2464±462	3.5		
ALMA-LAB18a	153^{+135}_{-40}	VLA-LAB18a	830±270	5.4	4.0	2.4
ALMA-LAB18b	355^{+313}_{-94}	VLA-LAB18b	586±254	1.7		
ALMA-LAB18d	575^{+508}_{-152}	VLA-LAB18d	1048±275	1.8		

[a] The star formation rates (SFRs) are determined from measured submm and radio fluxes under some assumptions (for details, see the text in § 3.3. 2σ upper limits are given for submm-undetected LABs. [b] Note that the LAB, not detected at dust and radio wavelengths but with X-ray emission, is also presented in this Table.